communications physics

ARTICLE

https://doi.org/10.1038/s42005-023-01440-5 OPEN

Ultrafast helicity-dependent photocurrents in Weyl Magnet Mn_3Sn

Dominik Hamara[1,4], Gunnar F. Lange[1,4], Farhan Nur Kholid[1], Anastasios Markou[2,3], Claudia Felser[2], Robert-Jan Slager[1✉] & Chiara Ciccarelli[1✉]

Mn_3Sn is a material that has attracted a lot of attention lately for its topologically non-trivial band structure, which leads to very promising spintronic properties. In this work we experimentally demonstrate that an epitaxially grown thin film of Mn_3Sn acts as a source of THz radiation at room temperature when irradiated by a femtosecond laser pulse. By combining various experimental measurements as a function of pump polarisation, magnetic field, and sample orientation we are able to explain the origin of the THz emission with the photocurrents generated via the photon drag effect. A thorough symmetry analysis combined with electronic band structure calculations using density-functional theory (DFT) are used to support our conclusions and provide a guide towards the important features that lead to photocurrent generation, which is useful for designing ultra-fast current pulses emitters.

[1] Cavendish Laboratory, University of Cambridge, J.J. Thomson Avenue, Cambridge CB3 0HE, UK. [2] Max Planck Institute for Chemical Physics of Solids, 01187 Dresden, Germany. [3] Physics Department, University of Ioannina, 45110 Ioannina, Greece. [4] These authors contributed equally: Dominik Hamara, Gunnar F. Lange ✉email: rjs269@cam.ac.uk; cc538@cam.ac.uk

Mn$_3$Sn is a noncollinear antiferromagnet (AF) and a Weyl semimetal (WSM). It crystallises in a hexagonal P6$_3$/mmc structure. Below the Néel temperature ($T_N \approx 420$ K for bulk Mn$_3$Sn[1]) the geometrical frustration of the Mn atoms in the a–b plane of the Kagome lattice leads to an inverse triangular spin structure, with 120° ordering[1–5]. Despite a vanishingly small net magnetisation, Mn$_3$Sn displays phenomena that conventionally occur in ferromagnets, such as a large anomalous Hall effect[6–8], anomalous Nernst effect[9], and magneto-optical Kerr effect[10]. This is possible due to the unique material topology and a nonzero Berry curvature resulting from the inverse triangular spin structure[1,8]. Ab-initio band structure calculations have reported the existence of multiple Weyl points in the bulk and corresponding Fermi arcs on the surface of Mn$_3$Sn[3]. An effect associated with WSMs is the presence of helicity-dependent photocurrents arising from non-linear optical effects. These have been observed using both electrical and THz techniques[11], and have been linked to the topological charge of the Weyl nodes[12], via the circular photogalvanic effect.

In this work, we present the observation of helicity-dependent ultrafast photocurrents in an 80 nm Mn$_3$Sn film at room temperature (RT) using optical pump-THz emisison spectroscopy. The experimental results obtained at different measurement geometries, temperatures, and external magnetic fields are cross-examined with theoretical predictions, allowing us to carefully verify specific mechanisms responsible for the generation of ultrafast photocurrents.

The magnitude and direction of the photocurrents depend on the polarisation of the pump pulse and the direction of its wavevector relative to the surface of the film, but have no dependence on magnetic field. These currents cannot be attributed to a bulk photogalvanic effect as this requires the breaking of inversion symmetry[13]. Mn$_3$Sn, however, respects inversion symmetry even when accounting for the magnetic ordering. This suggests that our signal originates either from a different bulk mechanism such as the inverse spin Hall effect[14] or photon-drag effect[15,16], or from a surface photogalvanic effect[17]. Our symmetry analysis of response tensors suggests that the helicity-dependent photocurrents arise predominantly due to the circular photon drag effect.

Results

Experimental layout. The subject of the study is an MgO(111) (0.5 mm)/Ru(5 nm)/Mn$_3$Sn(80 nm)/Si(3 nm) sample. In Fig. 1a, we show the optical pump-THz emission geometries used in our experiments. When presenting a data set we will refer to the experiment geometry in which this data was collected as *configuration 1*, *2* or *3*. To indicate different directions we introduce two Cartesian coordinate systems, also indicated in Fig. 1(a): (x, y, z)—fixed with respect to the experimental setup; (a, b, c)—fixed with respect to the sample. Laser pulses of 50 fs duration with a central wavelength of 800 nm propagate along the z-axis. A quarter-wave plate (QWP) placed in the pump path is used to control the polarisation and helicity of the pulses. In-plane rotations of the QWP by an angle φ allow changing between linear ($\varphi = 0° \pm n\pi/2$), left-handed circular (LHCP) ($\varphi = 45° \pm n\pi$), right-handed circular (RHCP) ($\varphi = -45° \pm n\pi$), and intermediate elliptical polarisations. The angle between the laser beam and the sample surface can be varied by rotating the sample away from normal incidence about the *x-axis* (*configuration 2*) or *y-axis* (*configuration 3*). We define the tilting angles as θ_x and θ_y respectively. Additionally, the sample can be rotated in-plane, about the c-axis by an angle defined as θ_c. An external magnetic field up to $\mu_0 H_x \approx 860$ mT can be applied along the x direction. Unless stated otherwise, the experiments presented in the main body of the paper were performed at room temperature (RT).

THz emission from Mn$_3$Sn. The optically induced charge currents $J_i(t)$ result in broadband THz electro-dipole emission $s_i(t)$. The subscript i indicates the polarisation components $i = x$ or $i = y$, along the two axes of the experimental setup x and y. As shown in Fig. S2 in Supplementary Note 2, THz transients detected from the Mn$_3$Sn sample switch the polarity upon changing the pump helicity from RHCP (right-hand circular polarisation) to LHCP (left-hand circular polarisation). This behaviour indicates the presence of pump-polarisation-dependent photocurrent generation mechanisms.

We define S_i as the integrated peak amplitude of the emitted THz pulse (we refer the reader to Fig. S2, S3 and S4 in Supplementary Notes 2 to 4 for a more precise definition in the different measurement configurations). Figure 1b shows the φ-dependence of S_y, measured at zero magnetic field ($\mu_0 H_x = 0$) and at normal pump incidence (*configuration 1*). The different polarisations of the pump pulse that correspond to the different values of φ are also indicated to facilitate the reading. The data is decomposed into different harmonics by fitting with the equation[18]:

$$S_i(\varphi) = H_i(\varphi) + L_i(\varphi) + B_i \tag{1}$$

Here, $H_i(\varphi) = h_i \sin(2\varphi + \varphi_1)$ is the magnitude of the circular polarisation helicity-dependent component with a phase shift φ_1, $L_i(\varphi) = l_i \sin(4\varphi + \varphi_2)$ is the linear polarisation-dependent component with a phase shift φ_2, and B_i is the polarisation-independent background component. As displayed in Fig. 1(c), the decomposition of S_y shows that $H_y(\varphi)$, $L_y(\varphi)$, and B_y all contribute to the measured signal. For comparison, S_x measured in the same experimental geometry (*configuration 1*) displays a relatively smaller contribution from the helicity-dependent $H_x(\varphi)$ component, and is dominated by $L_x(\varphi)$ (Supplementary Note 5). We attribute this difference to a small unintentional rotation around the y-axis, as it will be further justified in the analysis that follows. In our set-up, the sample's mount orientation can be freely adjusted around the y-axis, but not around the x-axis, so an unintentional tilting around the y-axis is more likely. In the following considerations, we focus on polarisation-dependent components of the signal, $H_y(\varphi)$, $L_y(\varphi)$. The remaining contribution, B_i does not have any dependence on optical polarisation, and can therefore be correlated to heating[19]. When the optical pump hits the sample surface its energy is absorbed by the electron bath and induces gradients in the electron temperature distribution at sub-picosecond timescales. The asymmetric diffusion of carriers along the gradient direction can lead to photo-currents. In our measurement layout, only the photocurrents generated parallel to the sample surface are radiative and can be detected. This is possible in the lateral photo-Dember effect[20], if the pump hits the sample close to one edge (we need to consider that the pump beam diameter is 1 mm, comparable to the sample size). This is also validated by the fact that the background value does not have any clear correlation with sample rotation angle, as shown in Table S1 in the Supplementary Note 6. We also exclude any magnetic field dependent effect such as the anomalous Hall effect because we do not observe any dependence on magnetic field or flipping of the sign when the magnetic field direction is flipped (please refer to the section *Magnetic field dependence* below and Supplementary Note 8).

The effect of experiment geometry. Here we study how both polarisation and amplitude of the photocurrent-generated THz emission depend on the direction of the optical wavevector q_z

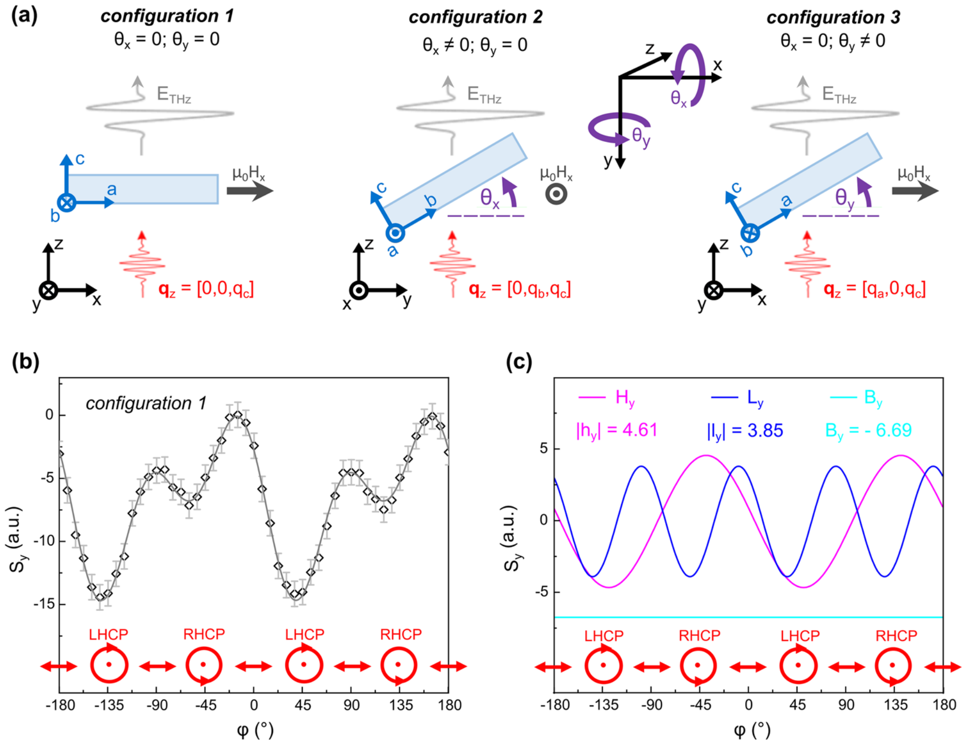

Fig. 1 Optical pump-THz emission from Mn_3Sn. a Experiment schemes in different geometries. Ultrafast laser pulses travelling along *z*-axis are incident on the sample, leading to the emission of broadband THz electro-dipole emission $s_i(t)$ with integrated peak amplitude S_i. In the experiments, we resolve the two orthogonal components of the transient THz signals: $s_x(t)$ and $s_y(t)$. θ_x, θ_y and θ_z label the rotation angles around the *x*, *y* and *z* axis respectively. *Configuration 1* corresponds to a measurement in the standard geometry with normal laser incidence, in which $\theta_x = 0$ and $\theta_y = 0$. In *configuration 2* and *configuration 3* the sample is rotated about the *x* ($\theta_x \neq 0$ and $\theta_y = 0$) or *y* ($\theta_x = 0$ and $\theta_y \neq 0$) axes respectively. Please note that the scheme of *configuration 2* is presented in a different perspective than *configuration 1* and *3*. **b** shows THz signals detected along *y*, emitted from Mn_3Sn optically pumped with laser pulses of different polarisations. The measurements were performed in *configuration 1* without an external magnetic field. The experimental data set is fitted with function introduced in Eq. (1) to find H_y, L_y, and B_y. Here, $H_i(\varphi) = h_i \sin(2\varphi + \varphi_1)$ is the magnitude of the circular polarisation helicity-dependent component with a phase shift φ_1, $L_i(\varphi) = l_i \sin(4\varphi + \varphi_2)$ is the linear polarisation-dependent component with a phase shift φ_2, and B_i is the polarisation-independent background component. These are presented in (**c**) with the extracted values of the amplitudes $|h_y|$, $|l_y|$, and B_y.

relative to the sample surface. For this purpose we tilt the sample whilst leaving the direction of the pump wavevector q_z unchanged with respect to the laboratory frame of reference, along the *z*-direction. For θ_x (*configuration 2*) or θ_y (*configuration 3*) different from zero, q_z has a non-zero projection along the *b* and *a* directions on the plane of the Mn_3Sn film, which we label q_b and q_a respectively. Consequently, the components of the wavevector relative to the sample frame are $[0, q_b, q_c]$ in *configuration 2* and and $[q_a, 0, q_c]$ in *configuration 3*.

Figure 2a and b show the components of the THz emission polarised along the *x* and the *y* directions as a function of φ, measured in *configuration 2* (a) and *configuration 3* (b). $S_x(\varphi)$ and $S_y(\varphi)$ are fitted with Eq. (1) to extract the coefficients h_x and h_y. While in Fig. 2a $h_x \gg h_y$, in Fig. 2b the trend is inverted and $h_x \ll h_y$. This suggests that the direction of the helicity-dependent photocurrent, and therefore of the THz polarisation, depends on the projection of the pump wavevector on the sample plane and is perpendicular to it. Due to finer control of θ_y in comparison to θ_x in our setup, we restrict the following analysis to *configuration 3* only. In Fig. 2c we show that the THz emission amplitude increases with tilting angle θ_y. We now study the symmetry of the THz emission for opposite tilting angles by decomposing $S_i(\varphi)$ into even and odd contributions as:

$$S_i(\varphi)_{even}(\theta_y = \pm 15^\circ) = S_i(\varphi)(\theta_y = +15^\circ) + S_i(\varphi)(\theta_y = -15^\circ) \quad (2)$$

$$S_i(\varphi)_{\mathrm{odd}}(\theta_y = \pm 15^\circ) = S_i(\varphi)(\theta_y = +15^\circ) - S_i(\varphi)(\theta_y = -15^\circ) \quad (3)$$

In Fig. 2d we observe that the odd component of S_y is dominant. Analogous behaviour is presented in Supplementary Note 7 for S_x. Our observations suggest that the helicity-dependent photocurrents are generated in the direction perpendicular to the in-plane projection of the pump wavevector and are proportional to it.

Magnetic field dependence. In this section we want to understand whether the photocurrents have a magnetic origin and depend on the magnetic phase of Mn_3Sn. Figure 3a shows S_y measured for two opposite directions of the magnetic field ±0.860 mT. According to Reichlova et al.[21], 0.860 mT may be too low to switch the magnetic ordering in Mn_3Sn thin films at RT, while it is sufficient to reverse the spins at temperatures close to T_N. Hence, for these measurements we followed a cool down procedure with the magnetic field continuously applied from 420 K to 380 K, at which the experiment was performed. No significant dependence on magnetic field is measured. We also do not observe a qualitative difference in the time-domain THz transients measured at different fields as shown in the SI.

We further confirm that the polarisation and amplitude of the emitted THz pulse is not correlated with the magnetic phase of Mn_3Sn by repeating the measurement after rotating the sample by 90° around the *c*-axis. Figure 3b shows $S_x(\varphi)$ and $S_y(\varphi)$ prior and after the rotation by $\theta_c = +90^\circ$. If the direction of the

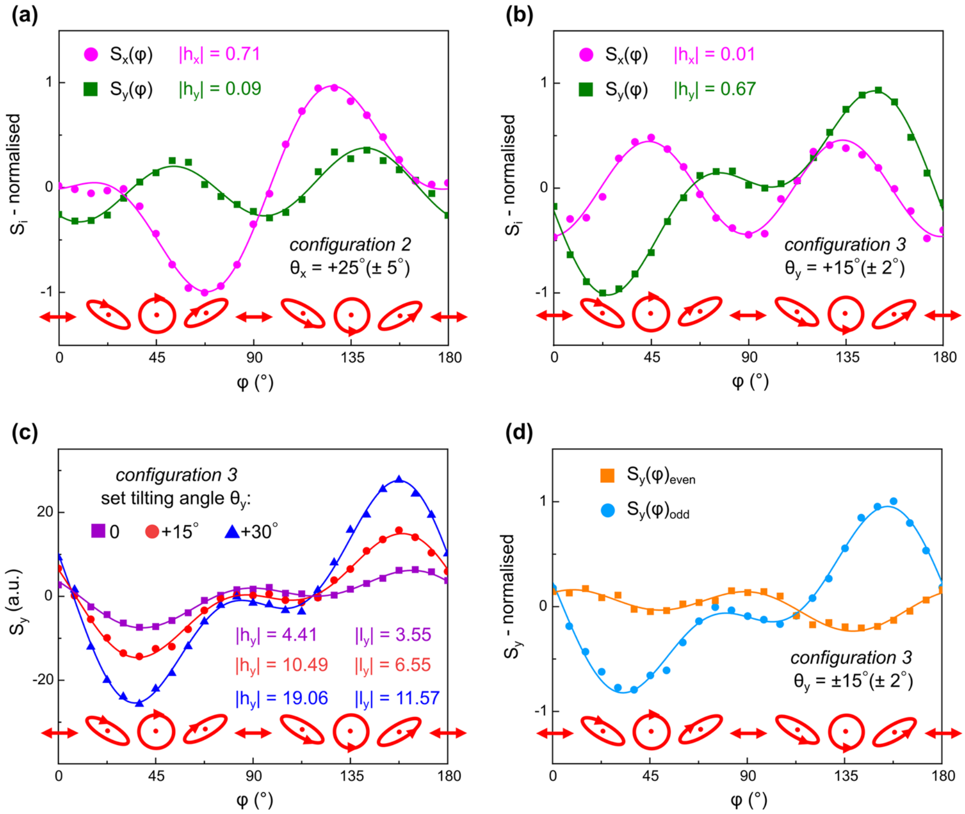

Fig. 2 Study of various experiment geometries in optical pump-THz emission from Mn_3Sn. Normalised THz emission amplitude $S_x(\varphi)$ and $S_y(\varphi)$ data sets measured in *configuration 2* and *configuration 3* are plotted in (**a**, **b**) respectively. The sample was rotated around the *x*-axis by $\theta_x = +25° \pm 5°$ or $\theta_y = +15° \pm 2°$ respectively. **c** shows THz signals measured along *y* in *configuration 3* for tilting angles θ_y between 0 and 30°. The data sets were fitted with Eq. (1) to extract the values of $|h_y|$ and $|l_y|$ parameters, respectively the magnitude of the circular polarisation helicity-dependent component and the near polarisation-dependent component. **d** shows even (see Eq. (2)) and odd (see Eq. (3)) responses with respect to θ_y, the rotation angle around the *y*-axis. The figure displays normalised THz signals measured along *y* in *configuration 3*. All measurements in (**a**–**d**) were performed at room temperature with no magnetic field. Data sets shown in (**a**, **b**–**d**) were fitted with Eq. (1) prior to normalisation to subtract the polarisation-independent backgrounds, B_i.

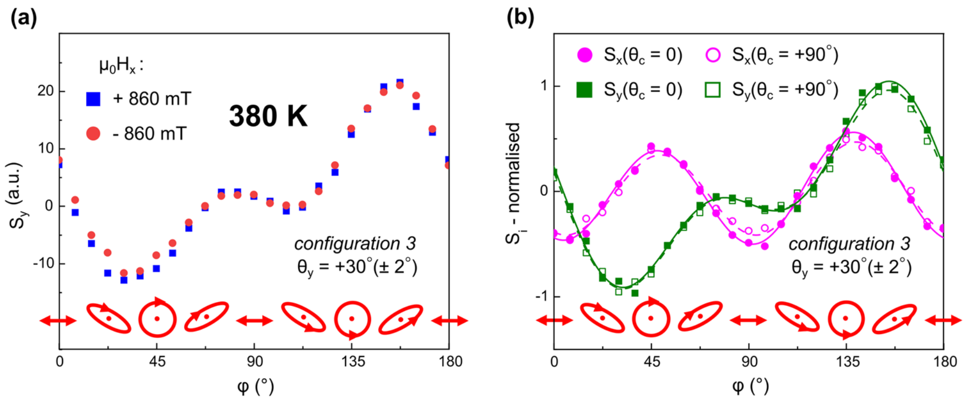

Fig. 3 Magnetic field dependence of THz emission from Mn_3Sn. a THz signals measured at 380 K in *configuration 3* after field-cooling from 420 K with opposite directions of external magnetic field continuously applied along *x*. **b** Normalised THz emission amplitude $S_x(\varphi)$ and $S_y(\varphi)$ data sets obtained prior, and after an in-plane rotation of the film by 90°. Prior to the measurements the sample was cooled down from 420 K to room temperature with the magnetic field of +860 mT. The field was switched off at room temperature, and $S_i(\varphi)(\theta_c = 0)$ were measured. Without repeating the field-cooling procedure and at zero magnetic field, the film was rotated in plane by +90° to obtain $S_i(\varphi)(\theta_c = +90°)$. The experiment was performed in *configuration 3*. The plots show normalised signal values. Prior to normalisation the data sets were fitted with Eq. (1) to subtract the polarisation-independent backgrounds, B_i.

photoinduced currents, hence the polarisation of the THz emission, were correlated with the orientation of the spins we would have expected a rotation of the THz polarisation plane by 90°, which we do not observe. Instead, the two graphs of $S_x(\varphi)$ and $S_y(\varphi)$ overlap, as is discussed further in the SI.

Theoretical analysis

Nonlinear optical effects. In this section, we investigate nonlinear optical effects in Mn_3Sn as an explanation of the observed signal. Other possible sources of helicity-dependent photocurrents are discussed in the subsequent section.

We consider a phenomenological expression for the induced photocurrent J_i that in turn generates THz emission via electro-dipole interaction. Using the notation from ref. [22] and expanding to second order in the light wave amplitude $E(\omega)$ for a frequency ω we write:

$$J_i = \chi^{(2)}_{ijk} E_j E^*_k + \chi^{(3)}_{ijkl} q_j E_k E^*_l \tag{4}$$

where all indices run over the Cartesian coordinates of the sample $i, j, k, l \in (a, b, c)$ and $\boldsymbol{q}$ is the momentum of the incoming light. At normal incidence (*configuration 1*), only q_c, E_a and E_b are non-zero. The first term describes the photogalvanic effect (PGE), whereas the second term describes the photon-drag effect (PDE). We further decompose each of these tensors into symmetric and antisymmetric components with respect to the light wave amplitude which respectively give rise to the linear photogalvanic/photon drag effect (LPGE/LPDE) and the circular photogalvanic/photon drag effect (CPGE/CPDE)[23]. Note that all quantitative features of these effects depend crucially on the details of the band structure. We show the ab-initio bulk and surface band structures in Fig. 4, for an energy-window of $\hbar\omega \approx 1.55$ eV, corresponding to the central wavelength of the laser pulses. Due to the large number of bands involved, we focus on a qualitative phenomenological symmetry analysis of the tensors in Eq. (4).

Symmetry-constrained model. The spatial symmetries of the material constrain the tensors in Eq. (4) and topology[24,25]. Mn_3Sn has space-group symmetry P6_3/mmc when ignoring magnetism and magnetic space-group symmetry C$m'cm'$ when including the AFM ordering[2]. For the tensor symmetry analysis, we focus on the unitary point-group symmetries as detailed in the SI, where also complete expressions for the symmetry-allowed forms of the PGE/PDE tensors in Eq. (4) are given. Here, we only summarise the number of independent coefficients for the various symmetry settings as shown in Table 1. In general, there are too many possible terms, making a quantitative model infeasible. However, by carefully comparing with our experimental results, it is possible to identify effects are the most relevant as detailed in the next section and in the Supplementary Note.

Interpretation of results. We begin by considering the effect of magnetism. As shown in Fig. 3a our results are insensitive to the direction and magnitude of the external magnetic field, as well as to the intrinsic spin ordering of the material [see Fig. 3b]. This suggests that the generated photocurrents do not arise as a result of the magnetic ordering in the material. We therefore focus on the non-magnetic symmetry analysis in what follows. Because the bulk of the sample respects inversion symmetry we should not expect any bulk contribution from the PGE in this case.

We address here the result of tilting the sample away from the normal pump incidence, as shown in Fig. 2. As discussed in detail in Supplementary Note 10, the tilting changes both what currents are generated in the material, and which part of the resultant THz radiation is measured at the detector. Tilting in θ_x (*configuration 2*) or θ_y (*configuration 3*) changes the geometry of the sample relative to the detector. In particular, we are able to resolve currents generated in the c-direction[26]. Thus, the detected integrated amplitude of the THz transient pulse in

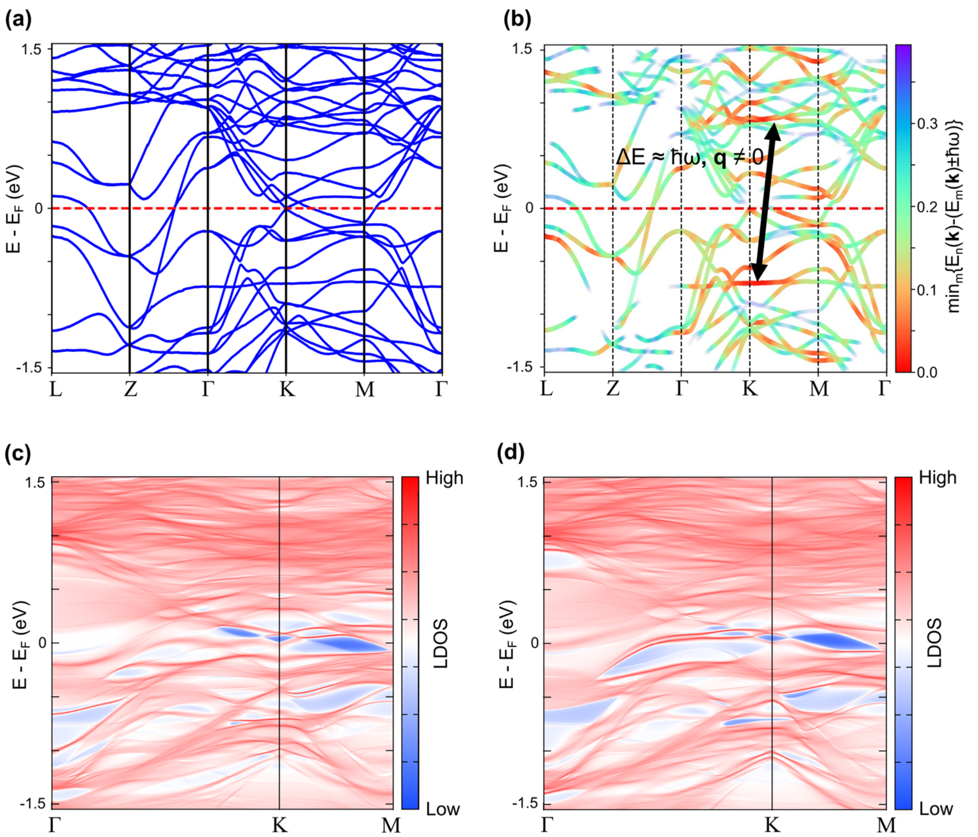

Fig. 4 Bulk and surface band structure for Mn_3Sn. In (**a**), we show the bulk band structure, for an energy window corresponding to the frequency of the laser. In (**b**), we show the same plot, but with the colour and opacity of the bands indicating the value of $\min_m\{E_n(\boldsymbol{k}) - (E_m(\boldsymbol{k}) \pm \hbar\omega)\}$ for band n, with $\pm$ indicating whether the band is above/below the Fermi surface. This is a rough indicator of the possibility of a vertical transition from band n occurring. The flat bands around K may also allow non-vertical transitions. In (**c**, **d**), we show the surface band structure for the c-directed top and bottom surface respectively, with the colour indicating how well-localised the states are on the surface.

Table 1 Number of independent elements for the linear/circular photogalvanic effect (LPGE/CPGE) and the linear/circular photon drag effect (LPDE/CPDE), for various unitary point-group (PG) symmetries relevant to the non-magnetic/magnetic (NM/M) bulk/surface of the material.

PG	Relevance	LPGE	CPGE	LPDE	CPDE
6/mmm	NM bulk	0	0	7	3
3m	NM surface	4	1	10	4
2/m	M bulk	0	0	28	13
1	M surface	18	9	54	27

configuration 2 is given by:

$$\begin{aligned} S_x &\propto J_a(\theta_x) \\ S_y &\propto J_b(\theta_x)\cos\theta_x + J_c(\theta_x)\sin\theta_x \end{aligned} \tag{5}$$

And in *configuration 3*:

$$\begin{aligned} S_x &\propto J_a(\theta_y)\cos\theta_y + J_c(\theta_y)\sin\theta_y \\ S_y &\propto J_b(\theta_y) \end{aligned} \tag{6}$$

Where the expressions for $J_i(\theta_k)$ arising from PGE/PDE are give in Supplementary Note 11. When considering the contribution from the bulk photon drag effect and the surface photogalvanic effect to $\boldsymbol{J}$, we find that all terms in the detected amplitude S_i arising from a bulk photon-drag effect are odd under tilting in both θ_x and θ_y, whereas the linear surface photogalvanic effect contains lowest-order terms that are even under tilting. We do not exclude the potential presence of the surface CPGE, which could be responsible for the even component of the signal. However, as the odd components make a significant contribution to our results (see e.g. Fig. 1c), we interpret our signal to arise predominantly from the bulk photon drag effect.

As discussed in Supplementary Note 11, we further find that the circular photon drag contribution to S_i normal to the rotation axis is suppressed, in agreement with the experimental results, and that only the bulk non-magnetic photon drag contribution is invariant under in-plane rotation [see Fig. 3b]. These observations indicate that the bulk photon drag effect is the main mechanism responsible for our signal.

In the photon drag effect, both angular and translational momenta are transferred from photons to the excited carriers. Therefore, this effect is linked to non-vertical transitions in momentum space[27,28]. As shown in Fig. 4b, Mn_3Sn has a flat bulk band below the Fermi energy around the K-point, with a corresponding band at a distance of $\hbar\omega$ corresponding to the energies of the optical excitation. This may lead to a large joint density of states, and allow for non-vertical transitions with finite $\boldsymbol{q}$. Hence, we note that the photon drag effect is also appealing from a bulk band-structure perspective.

Other possible sources of photocurrent. Another way in which helicity-dependent photocurrents can be generated is through a combination of the inverse Faraday effect (IFE) and inverse spin Hall effect (ISHE), as described recently for Bismuth thin-films in ref. [14]. This could be an important mechanism in Mn_3Sn, where effects related to the nonzero Berry curvature are significant[8] and may result in strong responses of the Faraday effect[29]. Furthermore, Mn_3Sn has been shown to have a large spin Hall angle[30]. However, we believe this mechanism does not play a significant role in our experimental results. Firstly, for an efficient conversion of IFE-induced spin currents into charge currents and THz electric fields the spins must travel relatively long distances[14]. This is not the case in Mn_3Sn, where the reported spin propagation length is below 1 nm[31]. Secondly, a Berry curvature related effect, such as the IFE, would show a strong dependence on the magnetic phase of Mn_3Sn. We do not observe this behaviour in our temperature measurements reported in Fig. S8 in Supplementary Note 9. Previous studies have reported that at temperatures above 420 K Mn_3Sn becomes paramagnetic and that upon cooling below RT the material can undergo transitions into the spiral and spin glass phases[1]. Our investigation in the temperature range of $50-400$ K does not reveal any abrupt changes in the magnitude of THz signals that could indicate the role of magnetic phase-dependent mechanisms. We do not, however, rule out that our sample remains in the same magnetic state over the entire investigated temperature range. Finally, the mechanism relying on the IFE and ISHE could only explain the helicity-dependent photocurrents and cannot account for the generation of photocurrents that show linear dependence on the pump polarisation. As shown in Fig. 1c, the magnitudes of H_y and L_y are comparable, and therefore we suggest their main contributions originate from related mechanisms, namely the CPDE and LPDE.

Conclusions

In conclusion, using optical pump-THz emission spectroscopy we present the generation of helicity-dependent ultrafast photocurrents in a Mn_3Sn thin film. The magnitude and direction of these can be fully controlled by the polarisation and incidence angle of the optical pump and are not affected by external magnetic fields. We combine the experimental results with theoretical analysis to suggest that the bulk photon drag effect is the main mechanism responsible for the generation of the helicity-dependent photocurrents.

Methods

The sample. Epitaxial Mn_3Sn films were grown using magnetron sputtering in a BESTEC ultra-high vacuum (UHV) system with a base pressure of $<2\times10^{-9}$ mbar and a process gas (Ar 5 N) pressure of 3×10^{-3} mbar. The target to substrate distance was fixed at 20 cm and the substrates were rotated during deposition to ensure homogeneous growth. The underlayer was deposited using a Ru (5.08 cm) target by applying 40 W DC power with the substrate held at 400 °C. Following cooling back to room temperature, Mn_3Sn was grown from Mn (7.62 cm) and Sn (5.08 cm) sources in confocal geometry, using 47 W and 11 W DC power respectively. The stack was then annealed in-situ under UHV at 350 °C for 10 min. The stoichiometry is $Mn_{75}Sn_{25}$ (±2 at. %), estimated by using energy dispersive x-ray spectroscopy (see Fig. S1 in Supplementary Note 1). Finally, a Si capping layer was deposited at room temperature using an Si (5.08 cm) target at 60 W RF power to protect the film from oxidation. Magneto-transport studies on films grown under the same conditions and with comparable crystal quality are presented in ref. [32] and show a large anomalous Hall effect at room temperature and a transition to topological Hall effect below 50 K.

Density-functional calculations. The electronic band structure was calculated using density-functional theory (DFT) as implemented in Quantum Espresso[33,34] with a fully-relativistic norm-conserving pseudopotential, generated using the ONCVPSP package[35]. We used the experimental crystal parameters $a = b = 5.67$ Å and $c = 4.53$ Å, with an $8\times8\times8$ **k**-grid and a kinetic-energy cutoff of 870 eV. The magnetic structure was relaxed by constraining the total direction of the magnetization. The bands were then Wannierised using Wannier90[36], with all d-orbitals of Mn considered in the projector. Finally, the slab band structure was computed using WannierTools[37].

Data availability

The datasets generated during and/or analysed during the current study are available in the Repository of the University of Cambridge Apollo at the address https://doi.org/10.17863/CAM.100540.

Received: 25 August 2023; Accepted: 24 October 2023;
Published online: 03 November 2023

References

1. Sung, N. H., Ronning, F., Thompson, J. D. & Bauer, E. D. Magnetic phase dependence of the anomalous hall effect in mn$_3$sn single crystals. *Appl. Phys. Lett.* https://doi.org/10.1063/1.5021133 (2018).
2. Brown, P. J., Nunez, V., Tasset, F., Forsyth, J. B. & Radhakrishna, P. Determination of the magnetic structure of Mn_3Sn using generalized neutron polarization analysis. *J. Phys. Condens. Matter* **2**, 9409–9422 (1990).
3. Yang, H. et al. Topological Weyl semimetals in the chiral antiferromagnetic materials Mn_3Ge and Mn_3Sn. *N. J. Phys.* **19**, 015008 (2017).
4. Li, X. et al. Momentum-space and real-space Berry curvatures in Mn_3Sn. *SciPost Phys.* **5**, 063 (2018).
5. Cheng, B. et al. Terahertz conductivity of the magnetic Weyl semimetal Mn_3Sn films. *Appl. Phys. Lett.* **115**, 012405 (2019).
6. Kübler, J. & Felser, C. Non-collinear antiferromagnets and the anomalous Hall effect. *Europhys. Lett.* **108**, 67001 (2014).
7. Nakatsuji, S., Kiyohara, N. & Higo, T. Large anomalous Hall effect in a non-collinear antiferromagnet at room temperature. *Nature* **527**, 212–215 (2015).
8. Nayak, A. K. et al. Large anomalous Hall effect driven by a nonvanishing Berry curvature in the noncolinear antiferromagnet Mn_3Ge. *Sci. Adv.* **2**, e1501870–e1501870 (2016).
9. Ikhlas, M. et al. Large anomalous Nernst effect at room temperature in a chiral antiferromagnet. *Nat. Phys.* **13**, 1085–1090 (2017).
10. Higo, T. et al. Large magneto-optical Kerr effect and imaging of magnetic octupole domains in an antiferromagnetic metal. *Nat. Photon.* **12**, 73–78 (2018).
11. Chan, C.-K., Lindner, N. H., Refael, G. & Lee, P. A. Photocurrents in weyl semimetals. *Phys. Rev. B* **95**, 041104 (2017).
12. de Juan, F., Grushin, A. G., Morimoto, T. & Moore, J. Quantized circular photogalvanic effect in Weyl semimetals. *Nat. Commun.* **8**, 15995 (2017).
13. Le, C. & Sun, Y. Topology and symmetry of circular photogalvanic effect in the chiral multifold semimetals: a review. *J. Phys. Condens. Matter* **33**, 503003 (2021).
14. Hirai, Y. et al. Terahertz emission from bismuth thin films induced by excitation with circularly polarized light. *Phys. Rev. Appl.* **14**, 064015 (2020).
15. Ribakovs, G. & Gundjian, A. A. Theory of the photon drag effect in tellurium. *J. Appl. Phys.* **48**, 4609–4612 (1977).
16. Maysonnave, J. et al. Terahertz generation by dynamical photon drag effect in graphene excited by femtosecond optical pulses. *Nano. Lett.* **14**, 5797–5802 (2014).
17. Steiner, J. F., Andreev, A. V. & Breitkreiz, M. Surface photogalvanic effect in Weyl semimetals. *Phys. Rev. Res.* **4**, 023021 (2022).
18. Ji, Z. et al. Spatially dispersive circular photogalvanic effect in a Weyl semimetal. *Nat. Mater.* **18**, 955–962 (2019).
19. Pettine, J. et al. Ultrafast terahertz emission from emerging symmetry-broken materials. *Light. Sci. Appl* **12**, 133 (2023).
20. Apostolopoulos, V. & Barnes, M. E. Thz emitters based on the photo-dember effect. *J. Phys. D Appl. Phys.* **47**, 374002 (2014).
21. Reichlova, H. et al. Imaging and writing magnetic domains in the non-collinear antiferromagnet Mn_3Sn. *Nat. Commun.* **10**, 5459 (2019).
22. Hamh, S. Y. et al. Helicity-dependent photocurrent in a Bi_2Se_3 thin film probed by terahertz emission spectroscopy. *Phys. Rev. B* **94**, 161405 (2016).
23. Karch, J. et al. Photon helicity driven electric currents in graphene. *arXiv* http://arxiv.org/abs/1002.1047 (2010).
24. Kruthoff, J., de Boer, J., van Wezel, J., Kane, C. L. & Slager, R.-J. Topological classification of crystalline insulators through band structure combinatorics. *Phys. Rev. X* **7**, 041069 (2017).
25. Schrunk, B. et al. Emergence of fermi arcs due to magnetic splitting in an antiferromagnet. *Nature* **603**, 610–615 (2022).
26. Ni, Z. et al. Giant topological longitudinal circular photo-galvanic effect in the chiral multifold semimetal CoSi. *Nat. Commun.* **12**, 1–8 (2021).
27. Shi, L.-k, Zhang, D., Chang, K. & Song, J. C. W. Geometric photon-drag effect and nonlinear shift current in centrosymmetric crystals. *Phys. Rev. Lett.* **126**, 197402 (2021).
28. Shalygin, V. A., Moldavskaya, M. D., Danilov, S. N., Farbshtein, I. I. & Golub, L. E. Circular photon drag effect in bulk tellurium. *Phys. Rev. B* **93**, 045207 (2016).
29. Yang, F., Xu, X. & Liu, R. B. Giant Faraday rotation induced by the Berry phase in bilayer graphene under strong terahertz fields. *N. J. Phys.* **16**, 043014 (2014).
30. Matsuda, T. et al. Room-temperature terahertz anomalous Hall effect in Weyl antiferromagnet Mn_3Sn thin films. *Nat. Commun.* **11**, 1–8 (2020).
31. Muduli, P. K. et al. Evaluation of spin diffusion length and spin hall angle of the antiferromagnetic Weyl semimetal Mn_3Sn. *Phys. Rev. B* **99**, 184425 (2019).
32. Taylor, J. M. et al. Anomalous and topological hall effects in epitaxial thin films of the noncollinear antiferromagnet Mn_3Sn. *Phys. Rev. B* **101**, 094404 (2020).
33. Giannozzi, P. et al. Quantum Espresso: A modular and open-source software project for quantum simulations of materials. *J. Phys. Condens. Matter* https://iopscience.iop.org/article/10.1088/0953-8984/21/39/395502 (2009).
34. Giannozzi, P. et al. Advanced capabilities for materials modelling with Quantum ESPRESSO. *J. Phys. Condens. Matter* https://iopscience.iop.org/article/10.1088/1361-648X/aa8f79 (2017).
35. Hamann, D. R. Optimized norm-conserving Vanderbilt pseudopotentials. *Phys. Rev. B* **88**, 085117 (2013).
36. Mostofi, A. A. et al. An updated version of wannier90: A tool for obtaining maximally-localised Wannier functions. *Comp. Phys. Commun.* **185**, 2309–2310 (2014).
37. Wu, Q., Zhang, S., Song, H.-F., Troyer, M. & Soluyanov, A. A. Wanniertools : An open-source software package for novel topological materials. *Comp. Phys. Commun.* **224**, 405–416 (2018).

Acknowledgements

C.C. and D.H. acknowledge support from the Royal Society. G.F.L. is funded by the Aker Scholarship. R.J.S. acknowledges funding from a New Investigator Award, EPSRC grant EP/W00187X/1, as well as Trinity college, Cambridge. G.F.L. thanks B. Peng, S. Chen, U. Haeusler and M.A.S. Martínez for useful discussions.

Author contributions

D.H. and C.C. planned the experiment; F.N.K. and D.H. built the experimental setup; D.H. took the measurements; G.FL. and R.J.S. provided theoretical modelling; D.H., G.F.L., R.J.S., C.C contributed to the analysis and interpretation of the data; A.M. and C.F. fabricated the samples and characterised them with XRD; D.H., G.F.L., F.N.K., A.M., C.F., R.J.S., C.C. drafted the manuscript; all authors discussed and commented on the manuscript.

Competing interests

The authors declare no competing interests.

Additional information

Supplementary information The online version contains supplementary material available at https://doi.org/10.1038/s42005-023-01440-5.

Correspondence and requests for materials should be addressed to Robert-Jan Slager or Chiara Ciccarelli.

Peer review information *Communications Physics* thanks the anonymous reviewers for their contribution to the peer review of this work. A peer review file is available.